PAPER

Check for updates

The resistive nature of decomposing interfaces of solid electrolytes with alkali metal electrodes†

Juefan Wang,[a] Abhishek A. Panchal,[a] Gopalakrishnan Sai Gautam [ID][b] and Pieremanuele Canepa [ID] *[ac]

A crucial ingredient in lithium (Li) and sodium (Na)-ion batteries (LIBs and NIBs) is the electrolyte. The use of Li metal (Na metal) as the anode in liquid electrolyte LIBs (NIBs) is constrained by several issues including thermal runaway, flammability, electrolyte leakage, and limited chemical stability. Considerable effort has been devoted toward the development of solid electrolytes (SEs) and all-solid-state batteries, which are presumed to mitigate some of the issues of Li metal (Na metal) in contact with flammable liquid electrolytes. However, most SEs, such as Li_3PS_4, Li_6PS_5Cl and Na_3PS_4 readily decompose against the highly reducing Li-metal and Na-metal anodes. Using first-principles calculations we elucidate the stability of more than 20 solid‖solid interfaces formed between the decomposition products of Li_3PS_4, Li_6PS_5Cl (and Na_3PS_4) against the Li-metal (Na-metal) electrode. We suggest that the work of adhesion needed to form a heterogenous interface is an important descriptor to quantify the stability of interfaces. Subsequently, we clarify the atomistic origins of the resistance to Li-ion transport at interfaces of the Li-metal anode and selected decomposition products (Li_3P, Li_2S and LiCl) of SEs, *via* a high-fidelity machine learning potential. Utilising an machine learning potential enables nano-second-long molecular dynamics simulations on 'large' interface models (here with 8320 atoms), but with similar accuracy to first-principles approaches. Our simulations demonstrate that the interfaces formed between Li metal and argyrodite (*e.g.*, Li_6PS_5Cl) decomposition products are resistive to Li-ion transport. The implications of this study are important since binary compounds are commonly found in the vicinity of the Li(Na) metal anode upon chemical and/or electrochemical decomposition of ternary and quaternary SEs.
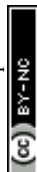
1 Introduction

Rechargeable lithium-ion batteries (LIBs) keep gaining importance for the development of next-generation energy storage devices and electric vehicles because of their outstanding gravimetric and volumetric energy densities.[1–5] Lithium metal batteries (LMBs) utilizing Li-metal anodes—that can achieve unprecedented energy densities theoretically, as compared to LIBs—have become one of the central topics of current research in rechargeable batteries.[4–6] The primary challenge in constructing practical LMBs is stabilizing the Li-metal‖electrolyte interface, with scientific studies mostly focused on identifying electrolyte formulations with limited reactivity and/or suitable additives.[1,5,7] Stabilizing the metal‖electrolyte interface is also a bottleneck in developing Na-metal batteries (NMBs).[4,5,8–10]

Solid electrolytes (SEs) are critical components in the development of LMBs and solid-state LIBs.[11–18] Besides acting as separators between electrodes, SEs are also expected to alleviate some of the safety issues between Li-metal anodes and liquid electrolytes.[4,5,19] Nevertheless, numerous reports have demonstrated high electrochemical instabilities of SEs when in contact with the Li-metal anode (and other electrode materials).[4] For example, sulfur-containing SEs are unstable against Li metal, resulting in the formation of undesired decomposition products, which may resist Li-ion transport and/or facilitate electron transport.[12–15,20–22] Thus, the stabilization of interfaces formed between Li metal (or other alkali-metal electrodes) and SEs remains a significant bottleneck in designing practical solid-state batteries.

Electrolyte decomposition occurs at small length scales away from the exteriors of the cell packs that constitute a battery. Therefore, the characterization of decomposition products in fully assembled and operating devices requires dedicated custom-made and expensive tools.[13,14,23,24] A number of reports have analyzed the compositions, structures, and formation mechanisms of the decomposing products of SEs against metal electrodes (metal electrode‖SE).[12–15,20–22] For example, X-ray photoemission spectroscopy (XPS) experiments by Wenzel

[a] Department of Materials Science and Engineering, National University of Singapore, 9 Engineering Drive 1, Singapore 117575, Singapore

[b] Department of Materials Engineering, Indian Institute of Science, Bangalore 560012, India

[c] Chemical and Biomolecular Engineering, National University of Singapore, 4 Engineering Drive 4, Singapore 117585. E-mail: pcanepa@nus.edu.sg

† Electronic supplementary information (ESI) available. See https://doi.org/10.1039/d2ta02202h

19732 | *J. Mater. Chem. A*, 2022, **10**, 19732–19742

This journal is © The Royal Society of Chemistry 2022

et al.[14] reported that Li_6PS_5X (with X = Cl, Br and I), upon contact with Li metal, forms Li_2S, LiX, and Li_3P. As a result, the decomposition products of metal electrode∥SE interfaces are expected to be multiphased and highly heterogeneous, which complicates the description of ionic transport across interfaces. Furthermore, the structures and properties of the metal electrode∥SE interfaces are expected to be markedly different from the bulk materials. A detailed study of the interfacial properties, particularly ionic transport is needed for the advancement of solid-state batteries.

Another aspect of solid-state batteries relates to the mechanical stability (*i.e.*, adhesion) of the solid∥solid interfaces that are chemically or electrochemically formed. The loss of contact due to the lack of adhesion between Li metal and SEs appears as a major cause driving the buildup of interfacial impedance in solid-state devices.[4,5,25] To evaluate the mechanical stabilities of the interfaces, Lepley and Holzwarth[26] have performed accurate first-principles calculations of several Li-metal∥SE interfaces (such as, Li∥Li_2O, Li∥Li_2S, Li∥Li_3PO_4 and Li∥Li_3PS_4) and found that all interfaces were stable except Li∥Li_3PS_4. Other studies have investigated the effects of the stability of heterogeneous interfaces on the Li-ion transport properties.[27–29]

Yang and Qi[27] have proposed that an interface with good adhesion, *i.e.* a "lithiophilic interface" can result in a faster critical stripping current density, which is crucial to prevent dendrite growth. Recently, Seymour and Aguadero[28] have shown that Li (or Na)-ion transport across alkali-metal∥SE interfaces correlates directly with interfacial adhesion. Yang *et al.*[29] have employed classical molecular dynamics (MD) to study the process of Li plating and stripping on solid Li_2O, showing that a coherent interface with strong interfacial adhesion and fast Li-ion diffusion can prevent pore formation at the interface. Here, we perform a systematic investigation including a larger data set of solid∥solid interfaces, particularly focusing on the correlation between the atomistic structure of interfaces and ionic transport, which is presently lacking.

We address the interfacial stability and Li-ion mobility of multiple interfaces formed between the Li-metal electrode and decomposition products of topical SEs, such as, Li_3PS_4,[15,26,30,31] argyrodite-Li_6PS_5Cl[14] and LiPON, with general formula Li_xPO_y-N_z.[23,24,32] We also analyze the Na∥Na_2S and Na∥Na_3P interfaces, which form upon the decomposition of Na_3PS_4 against Na metal.[13] We perform large-scale MD simulations of selected interfaces, (*i.e.*, Li∥Li_3P, Li∥Li_2S and Li∥LiCl) based on high-fidelity machine learning potentials (MLPs) trained on accurate first-principles data, which carry the accuracy of *ab initio* molecular dynamics (AIMD) while giving access to appreciably larger time and length scale simulations.

We reveal that the mechanical stabilities of the Li (or Na)-metal∥SE interfaces are primarily governed by the atomistic structures of the interfaces, which in turn are dependent on the surface orientations and/or terminations of the decomposition products. Furthermore, we show that the interfaces formed between Li metal and decomposition products of the argyrodite Li_6PS_5Cl SE (*i.e.*, Li_3P, Li_2S and LiCl) are resistive to Li-ion transport, explaining the observed impedance buildup. Our

results provide insights into engineering solid∥solid interfaces with better interfacial stability and improved ionic transport.

2 Construction of interfaces of decomposition products and metal anodes

We discuss the procedure to build heterogeneous interfaces between an alkali metal (Li or Na) with one of their binary compounds (*e.g.*, Li_3P), formed as a result of SE decomposition. In constructing the heterogeneous interfaces between the alkali metal (*e.g.*, Li or Na) and the binary compounds, we identify stable stoichiometric surfaces (following Tasker's criteria[33]) with low surface energies, γ, of both materials, which are paired into an interface (see Table S1 of the ESI†). To describe γ, we have used the slab model in eqn (1).[34]

$$\gamma = \lim_{N \to \infty} \frac{1}{2S} \left[E_{slab}^N - N E_{bulk} \right] \quad (1)$$

where S is the surface area of the slab, E_{slab}^N is the energy of the relaxed slab containing N formula units, and E_{bulk} is the energy per formula unit of the bulk structure. The energies of eqn (1) (and the following equations) are Gibbs energies, which we approximated by using density functional theory (DFT, see Sec. 7) total energies ignoring pV and entropic contributions. The slab models included a sufficient number of layers and a vacuum of 15 Å was used to converge γ to within ±0.01 J m^{-2}.

The set of stable surfaces in Li (or Na)-metal and binary compounds are considered, and their corresponding γ values are displayed in the Wulff shapes shown in Fig. 1.[35,36] The values of γ, not shown in Fig. 1, are included in Tables S2 and S3 of the ESI.† The (100) surface of Li metal has the lowest surface energy of ∼0.46 J m^{-2}, while for Na metal, the (100) and (110) surfaces have similar γ values, ∼0.22 J m^{-2} and ∼0.21 J m^{-2}. In Li_2S, Li_2O, Na_2S, and Na_2O, the (111) facet dominates the Wulff shape, while for Li_3P, LiCl, Li_3N, and Na_3P, the {001}-type surfaces have the lowest γ values (Fig. 1). Our calculated surface energies, ∼0.33 J m^{-2} for the (111) surface and ∼0.51 J m^{-2} for the (110) surface of Li_2S, as well as ∼0.53 J m^{-2} for the (111) surface of Li_2O are consistent with the values reported in previous literature studies.[37,38] Li_3N and LiCl exhibit stable facets that are terminated with both Li and anion species, while other compounds have stable facets exposing a Li (or Na) layer.

The surfaces shown Fig. 1 are subsequently paired to form heterogeneous interfaces. Different metrics serve to quantify the effect of mechanical strain and/or the chemical bond formation/destruction at the interface.[39,40] The interface formation energy (E_f calculated using eqn (2)) is the energy difference between the interface model and bulk structures of A and B, and includes both mechanical (*i.e.*, elastic strain) and chemical components.[34]

$$E_f = \frac{E_{AB} - [N_A E_A + N_B E_B]}{2S} \quad (2)$$

where S is the surface area of the interface and E_{AB} is the energy of the fully relaxed interface model, containing N_A and N_B
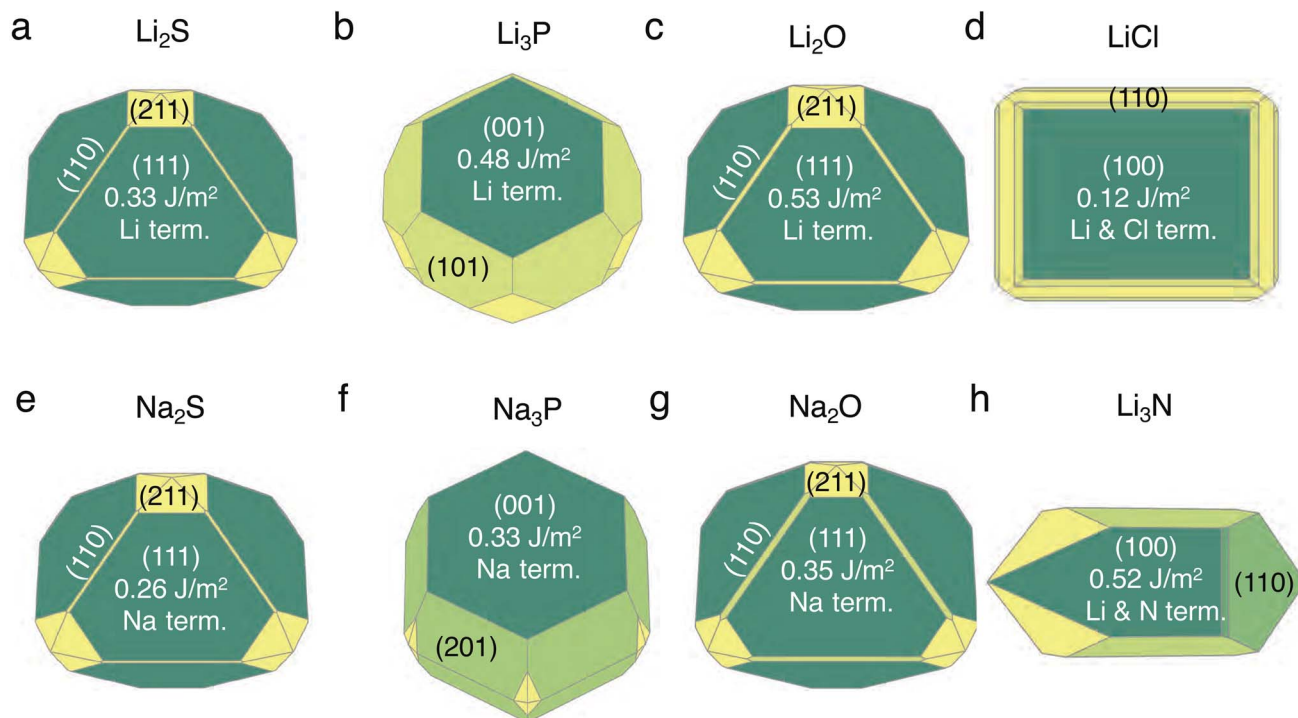
This journal is © The Royal Society of Chemistry 2022

J. Mater. Chem. A, 2022, **10**, 19732–19742 | 19733

Fig. 1 Computed Wulff shapes of binary compounds Li_2S (panel a), Li_3P (b), Li_2O (c), LiCl (d), Na_2S (e), Na_3P (f), Na_2O (g), and Li_3N (h), with their corresponding surface energies (in J m^{-2}). The chemical nature of the surface terminations (term.) are also indicated. Wulff polygons are constructed using stoichiometric, non-polar, and symmetric surfaces (including an inversion symmetry).

formula units of materials A and B, whose bulk energies are E_A and E_B, respectively. Elastic stress can arise in interfaces displaying large lattice mismatch, and "absorbed" by the interface through the release of the stress energy, *via* formation of dislocations.[41,42] By removing the elastic strain from E_f (of eqn (2)), we obtain two important descriptors: (i) the interfacial energy, σ of eqn (9), and (ii) the work of adhesion, $W_{adhesion}$ of eqn (4), which are paramount in evaluating the overall stability of interfaces. σ quantifies the formation (or destruction) of chemical bonds as the interface is created, excluding all mechanical contributions.

$$\sigma = \frac{E_{AB} - \left[N_A E_{A(z)} + N_B E_{B(z)}\right]}{2S} \quad (3)$$

where $E_{A(z)}$ and $E_{B(z)}$ are the energy per formula unit of the bulk A and B, as obtained from a constrained relaxation along the direction (z) normal to the interface, where the in-plane lattice vectors of the bulk structures are fixed to those of the fully relaxed interface. It follows that, the elastic strain energy associated with the interface is calculated as $E_f - \sigma$.

The work of adhesion, $W_{adhesion}$ (of eqn (4)) is the work done to part two adherent surfaces to an infinite distance, and quantifies the mechanical stability of an interface.

$$W_{adhesion} = \gamma_A + \gamma_B - \sigma \quad (4)$$

where γ_A and γ_B (eqn (1)) are the surface energies of materials A and B, respectively. Nominally, small (positive) values of σ and large (positive) values of $W_{adhesion}$ are indicative of a high

interfacial stability. To account for the effect of elastic strain, eqn (5) gives an alternative definition of $W_{adhesion}$.

$$W_{adhesion} = \gamma_A + \gamma_B - E_f \quad (5)$$

For the creation of interface models, we use the algorithm by Taylor *et al.*,[43] which samples the configurational space to find interface models that minimize the lattice mismatch between two materials. While pairing surfaces, we used the in-plane lattice constants of the binary compounds (*e.g.*, Li_3P) and applied a lattice mismatch-induced strain to the metal surface, since the bulk moduli of binary compounds are typically greater than the alkali metals (*i.e.*, Li and Na).[11,44] The constructed interface models are symmetric; for example, $Li_2S\|Li$-metal consists of two identical interfaces that forms a $Li_2S\|Li$-metal$\|Li_2S$ system, as displayed in panel c in Fig. 2. The slab thickness of binary compounds is typically $\sim$10 Å, which is sufficient to distinguish the interface features from their bulk-like properties. However, thicker slabs are required for Li ($\sim$12 Å) and Na ($\sim$14 Å) to distinguish the interface regions from the bulk region.[26]

3 Stability of interfaces of decomposition products and metal electrodes

Fig. 2a and b show the computed interfacial energetics, E_f, σ, and $W_{adhesion}$ (as defined in eqn (4)), for a number of interfaces

19734 | *J. Mater. Chem. A*, 2022, **10**, 19732–19742

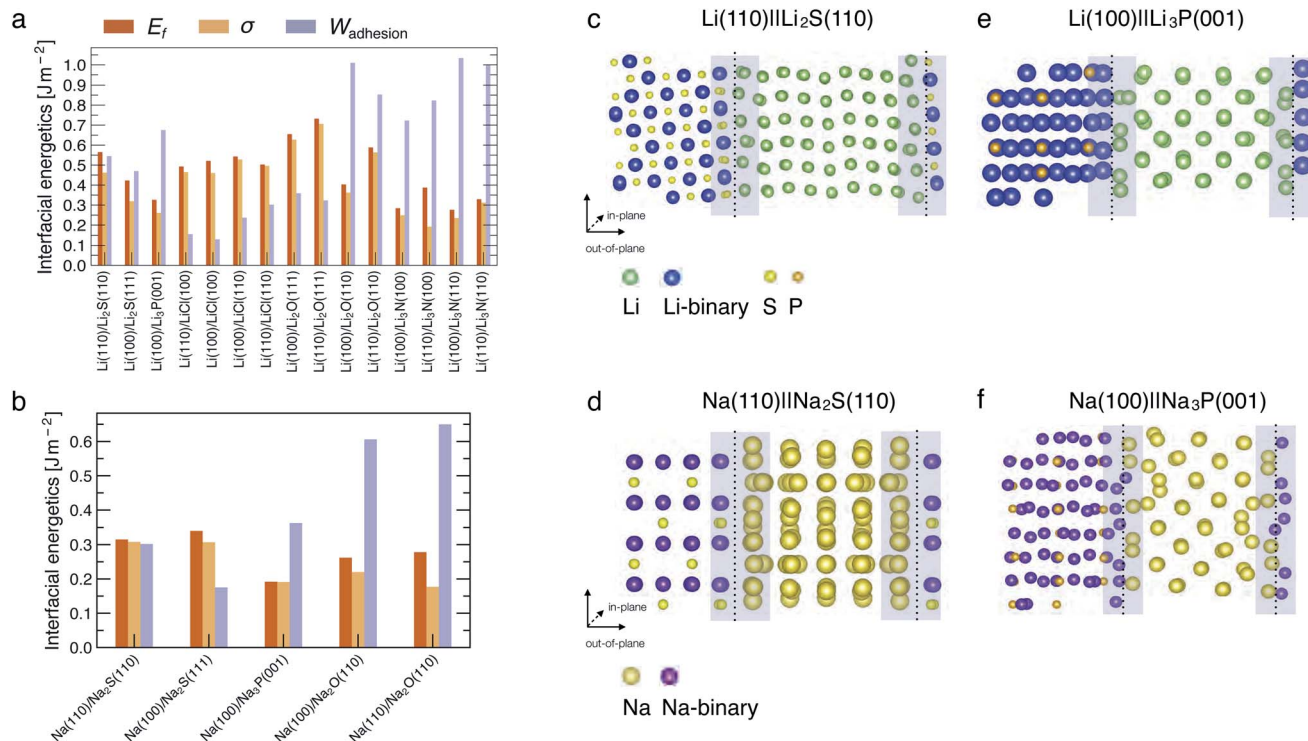This journal is © The Royal Society of Chemistry 2022

Fig. 2 Computed interfacial quantities (in J m^{-2}) for (a) Li-based interfaces and (b) Na-based interfaces. Atomic structures of representative interfaces, namely (c) Li(110)‖Li$_2$S(110), (d) Na(110)‖Na$_2$S(110) (e) Li(100)‖Li$_3$P(001) and (f) Na(100)‖Na$_3$P(001). The interface regions are indicated by the shaded areas. The non-periodic direction of the interface is indicated by the "out-of-plane" vectors.

considered. An illustration of the interface models for Li(110)‖ Li$_2$S(110), Na(110)‖Na$_2$S(110), Li(100)‖Li$_3$P(001) and Na(100)‖ Na$_3$P(001) is shown in Fig. 2c–f, where the interfacial regions are indicated by the shaded areas. Representations of other interfaces are shown in Fig. S1–S5 of the ESI.† In the Li cases considered, we find the most stable interfaces are those formed with Li$_3$N, displaying $W_{adhesion}$ in the range of 0.8–1.0 J m^{-2}, and $\sigma \sim 0.25$ J m^{-2} (Fig. 2a). In contrast, the least stable interfaces are Li‖LiCl, which exhibit a low $W_{adhesion}$ and high σ. In Na-based systems, the most and least stable interfaces are Na(110)‖ Na$_2$O(110) and Na(100)‖Na$_3$P(001), respectively. Note that results of $W_{adhesion}$ from eqn (5) (including strain contributions) in Fig. S7 and S8† appear similar in magnitude (and sign) to those obtained using eqn (4) (excluding strain) in Fig. 2. Therefore, we will refer to $W_{adhesion}$ of eqn (4) and Fig. 2 throughout the remainder of the manuscript.

Previous computational and experimental studies have suggested that Li‖Li$_2$S, Li‖Li$_3$P and Li‖LiCl interfaces are expected to form when argyrodite-Li$_6$PS$_5$Cl SE reacts with Li metal.[14,15] A comparison of the $W_{adhesion}$ (Fig. 2a) of these interfaces indicates that Li‖LiCl ≪ Li‖Li$_2$S < Li‖Li$_3$P. Li(100)‖Li$_3$P(001) is expected to dominate the overall interface of Li metal and Li$_6$PS$_5$Cl, if similar quantities of Li$_2$S and Li$_3$P are produced upon decomposition. In the case of Li$_3$PS$_4$, predicted values of $W_{adhesion}$ (Fig. 2a) suggest the coexistence of both Li‖Li$_2$S and Li‖Li$_3$P interfaces, consistent with prior literature studies.[15,45,46] For LiPON, $W_{adhesion}$ follows the order Li‖Li$_3$P ≪ Li‖Li$_2$O ≈ Li‖Li$_3$N, implying that the Li-metal anode will mostly interface

with Li$_2$O and Li$_3$N, also consistent with previous investigations.[15,23,24,32,47]

In most cases considered, the interfacial region (shaded regions in Fig. 2c and d) exhibits substantial atomic rearrangements upon full relaxation, with the exceptions being Li(110)‖Li$_3$N(110) (Fig. S3†) and Li(110)‖LiCl(100) (Fig. S2†). A qualitative analysis of the interface models suggests that there is always a pronounced atomic reconstruction on the metal side of the interface as compared to that of the binary compound for all Li (and Na) interfaces. This is another confirmation that both Li and Na metals are softer than their binary compounds.[44] Li (or Na) atoms originating from the metal side of the interfacial region form stabilising bonds with anion species from the compound side, with bond lengths that are similar to the bulk binary structures (see Table S5†).

In general, interfaces with a lattice mismatch smaller than a few percent can be considered as epitaxial, and the re-organization of atoms at the interface remains minimal compared to others with a significant lattice mismatch ($\geq$5%). In some cases, we find large lattice mismatches when interfaces are formed between the dominant facets of binary compounds with the (100) or (110) surfaces of the metals (Li or Na). For example, the Li$_2$S(111) facet displays a lattice mismatch of $\sim$14.2% with the Li(100) surface (Table S3†), indicating that such an interface may not occur practically. The lattice mismatch between Li$_2$S(110) and Li(110) facets is lower ($\sim$5.1%) and consequently exhibits a higher $W_{adhesion}$ than Li$_2$S(111)‖Li(100). The Li$_2$S‖Li interface is likely to exhibit significant structural re-

This journal is © The Royal Society of Chemistry 2022

J. Mater. Chem. A, 2022, **10**, 19732–19742 | **19735**

arrangement since the $Li_2S(110)$ facet does not occupy a significant portion of the Wulff volume of Li_2S, and consequently results in a $Li_2S\|Li$ interface that is susceptible to delamination in real devices.

We also find that the surface terminations of binary compounds are crucial to determine the interfacial stability. For example, the $Li(110)\|Li_2O(111)$ interface has a small lattice mismatch of $\sim1.73\%$ (Table S3†). However, its fully relaxed geometry exhibits larger lattice distortion of the interfacial region as compared to other $Li\|Li_2O$ based interfaces (see Fig. S4†). This interfacial instability comes from the fact that the $Li_2O(111)$ surface is terminated with only Li atoms—this excess number of Li atoms and lack of anions near the interface region affects the chemical stabilization of the interface due to the lack of bond formation between Li (from the metal side of the interface) and O.

In Na systems, the $Na(110)\|Na_2S(110)$, $Na(100)\|Na_2S(111)$, and $Na(100)\|Na_3P(001)$ show reconstructions in the interfacial region similar to their Li analogues (Fig. 2c and S1c, d†). Additionally, we find the computed values of $W_{adhesion}$ (and σ) to be lower (less positive) than their corresponding Li analogues (see Fig. 2a and b). Despite the low values of $W_{adhesion}$ (<0.35 J m^{-2}), both $Na\|Na_2S$ and $Na\|Na_3P$ may still occur at the Na-metal electrode. The $Na\|Na_2O$ interface has a significantly larger $W_{adhesion}$ (~0.65 J m^{-2}) than $Na\|Na_3P$ (~0.35 J m^{-2}) and $Na\|Na_2S$ interfaces (~0.30 J m^{-2}).

4 Lithium transport at heterogeneous interfaces

To quantify ionic transport through heterogeneous interfaces, we have used the tracer diffusivity, D^* of eqn (6) and (7). While we quantify only Li-ion transport across heterogeneous interfaces, similar qualitative trends might hold for Na-ion transport as well.

$$D^*(T) = \lim_{t \to \infty} \frac{1}{2dt} \frac{1}{N} \sum_{i=1}^{N} \left\langle |r_i(t) - r_i(0)|^2 \right\rangle; \qquad (6)$$

$$D^*(T) = D_0 \exp\left(-\frac{E_a}{k_B T}\right). \qquad (7)$$

where $r_i(t)$ is the displacement of the ith Li-ion at time t, N is the number of diffusing ions, and d is the dimensionality of the diffusion process. E_a in the Arrhenius eqn (7) is the Li-ion migration energy, D_0 is the ionic diffusivity at infinite temperature (T), and k_B is the Boltzmann constant. We obtain D^*, D_0 and E_a from MD simulations based on our trained moment tensor potentials (MTPs),[48] which is machine learned from AIMD simulations of the bulk and interface structures (see Sec. 7.2). The largest MD simulations of heterogeneous interfaces investigated in this study contains 8320 atoms and samples the ionic dynamics for times >10 ns, which enables an accurate assessment of transport properties. Table S6† summarizes the mean absolute errors from the MTP training and its validation.
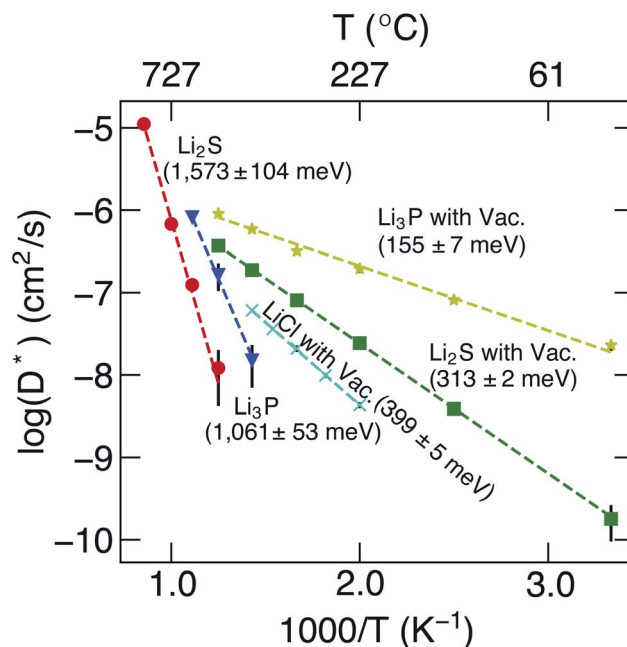

Fig. 3 Arrhenius plots of Li^+ D^* (in cm^2 s^{-1}) of bulk binary compounds from MTP-MD simulations. The activation energies, calculated from eqn (7), and the related error bars are provided as text annotations. Vac. stands for structures with a Li vacancy.

The calculated D^* as a function of temperature for bulk binary compounds Li_2S, Li_3P and LiCl, with and without Li^+ vacancies (Vac) are shown in Fig. 3. We have not included the case of LiCl without vacancies where we could only probe a limited number of diffusion events, which are insufficient to estimate accurate Li-ion diffusivities. The assessment of Li-ion transport in the bulk structures of Li_2S, Li_3P and LiCl is crucial to compare the transport across heterogeneous interfaces. Notably, our calculated E_a is in reasonable agreement with the experimental results (see Table S7†). For example, the calculated E_a in LiCl with Vac, ($\sim399 \pm 5$ meV), is qualitatively similar to the existing experimental value (~510 meV).[49] The computed E_a of Li_3P with Vac ($\sim155 \pm 7$ meV) is in better agreement with the experiment value (~180 meV)[50] as compared to pristine Li_3P ($\sim1061 \pm 53$ meV). On the other hand, the calculated E_a in pristine-Li_2S ($\sim1573 \pm 104$ meV) is closer to the experimental value (~1.5 eV at $T > 800$ K)[51] than the calculated E_a in Li_2S with Vac ($\sim313 \pm 2$ meV). Unsurprisingly, the introduction of Vac lowers the activation energies of both Li_2S and Li_3P as shown in Fig. 3. The calculated E_a of Li_3P (with Vac) is lower than that of Li_2S (with Vac), which is in agreement with previous studies showing superior Li-ion conductivity of Li_3P over Li_2S.[52]

To investigate the Li-ion transport across the argyrodite-$Li_6PS_5Cl\|Li$-metal interface (*i.e.*, the interfaces formed by the decomposition products of argyrodite with Li metal), we performed MTP-MD simulations on three interface models, namely, $Li(110)\|Li_2S(110)$, $Li(100)\|Li_3P(001)$ and $Li(110)\|LiCl(100)$. The choice of these specific interfaces is motivated by their highest $W_{adhesion}$ values (Fig. 2a) compared to other possible configurations using Li metal and the same binary compound. Although $Li(110)\|LiCl(110)$ has the highest

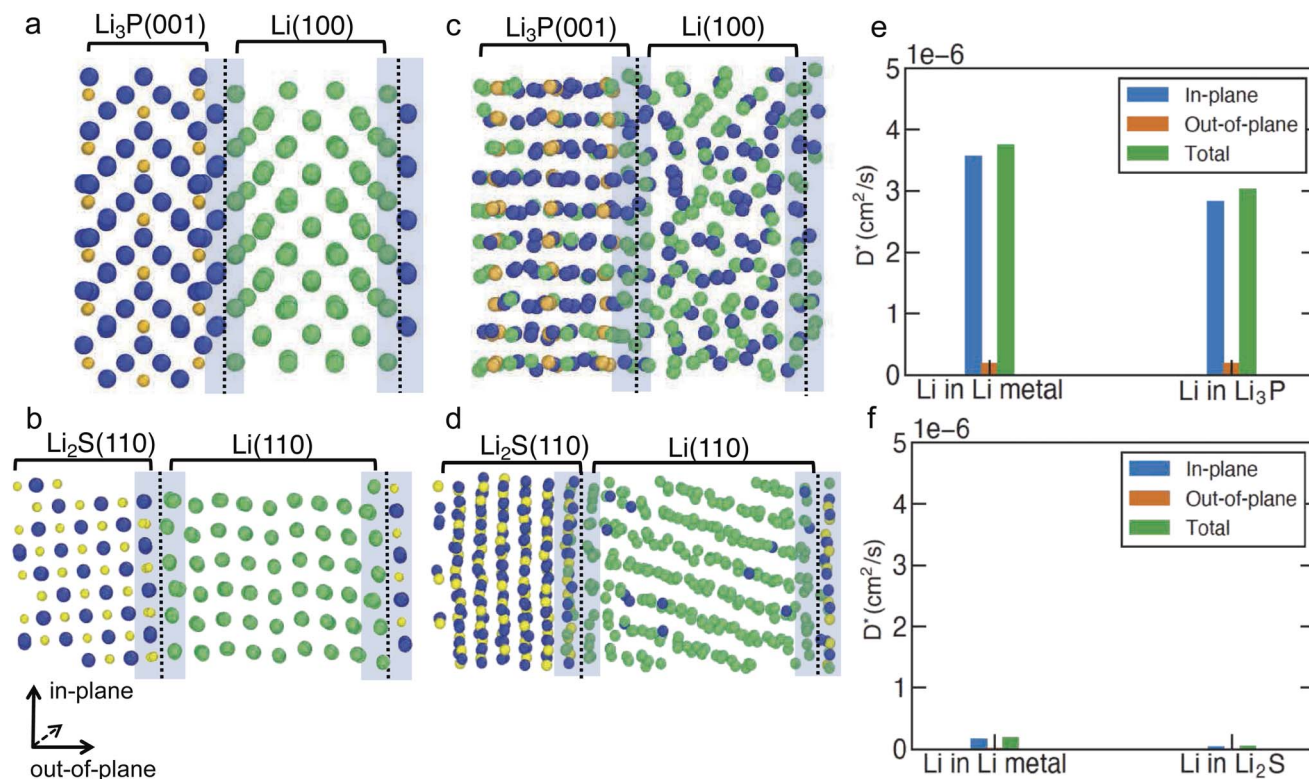**19736** | *J. Mater. Chem. A*, 2022, **10**, 19732–19742

This journal is © The Royal Society of Chemistry 2022

Fig. 4 Snapshots of (a, c) Li(100)‖Li$_3$P(001) and (b, d) Li(110)‖Li$_2$S(110) interfaces at 0 ns (a and b), and 5 ns (c and d), respectively, at 400 K. The in-plane and out-of-plane components of Li$^+$-D^* in the Li-metal and Li$_3$P regions (e) of the Li(100)‖Li$_3$P(001) interface and Li$_2$S regions (f) of the Li(110)‖Li$_2$S(110) interface at 400 K. Dark blue spheres: Li$^+$ (binary), green spheres: Li$^+$ (metal), orange spheres: P and yellow spheres: S.

$W_{adhesion}$, we have chosen Li(110)‖LiCl(100) as the representative model because of its lower computational cost for AIMD simulations. We randomly introduced a number of Li$^+$ vacancies (~1.1%) into the interface region to calculate D^*, since it is likely that heterogeneous interfaces will comprise highly defective materials, especially due to the *in situ* formed decomposition products. To distinguish Li$^+$ belonging either to Li metal or binary compounds, we have labeled Li$^+$ in Li metal as Li$^+$ (metal) (green spheres in Fig. 4 and S9†), and Li$^+$ in binary compounds as Li$^+$ (binary) (dark blue spheres), respectively. Furthermore, the direction of Li-ion transport with respect to the interfacial plane, *i.e.*, in-plane or out-of-plane, helps to qualify the nature of Li transport. Indeed, only Li ions diffusing out-of-plane will contribute to effective ion-transport across the interface. The predicted Li$^+$-D^* in both Li metal and binary compounds are summarized in Table S8.† The mean square displacement (MSD) plots used to derive Li$^+$-D^* are shown in Fig. S11–S13.†

In Fig. 4a–d and S9a, b,† we show the snapshots of different interfaces at 400 K during the MTP-MD simulations. In the following paragraphs, bulk is intended as the portion of the interface model which mimics the bulk structure. Initially, all interfaces exhibit modest atomic rearrangements near the interface region (violet shaded area). After ~5 ns, significant Li$^+$ displacement in both the metal and binary bulk along with Li$^+$ exchange (*i.e.*, there is a significant amount of Li$^+$ (metal) diffusing into Li$_3$P bulk and *vice versa*) can be clearly observed in Li(100)‖Li$_3$P(001). This can be understood by the high values of

Li$^+$-D^* (Fig. 4e) in both the in-plane (within bulk systems, 3.03×10^{-6} to 3.76×10^{-6} cm^2 s^{-1}) and out-of-plane (across the bulk systems, 1.93×10^{-7} to 1.99×10^{-7} cm^2 s^{-1}) directions in the Li(100)‖Li$_3$P(001) system.

In contrast, in Li(110)‖Li$_2$S(110) and Li(110)‖LiCl(100), we observe limited diffusion events and sparse exchange of Li ions during the MTP-MDs, which in turn is quantified by the low in-plane (4.86×10^{-8} to 1.89×10^{-7} cm^2 s^{-1}) and even lower out-of-plane (6.43×10^{-9} to 2.21×10^{-8} cm^2 s^{-1}) diffusivities in both systems. We find that for all interfaces, the out-of-plane components of both Li$^+$ (metal) and Li$^+$ (binary) are much smaller than their respective in-plane components, which indicate that the Li$^+$ diffusion across the interface remains limited.

5 Discussion

A systematic study of the structures, interfacial energetics, and ionic transport properties of solid/solid interfaces is paramount for the development of solid-state batteries. Here, we have used a combination of accurate DFT calculations to explore the stability of interfaces arising from the decomposition of SEs with highly reducing alkali-metals, *i.e.*, Li and Na. Upon identifying the thermodynamically stable heterogeneous interfaces, we trained MTPs based on accurate AIMD simulations, and in turn used such MTPs to run long duration (>10 ns) simulations to elucidate the Li-ion transport properties across specific interfaces.

This journal is © The Royal Society of Chemistry 2022

J. Mater. Chem. A, 2022, **10**, 19732–19742 | **19737**

Although the morphology of real electrode‖SE interfaces can be far more complex than the interface models used here, our detailed atomistic models provide insights into the microscopic structure and mechanical stability of buried interfaces between SEs and alkali-metals. Still, one major limitation of our analysis is the finite number of interface models considered (20 in this study). Clearly, it is impossible to survey the whole configurational space of interfaces (potentially thousands[11,16,34]), and alternative strategies should be sought.

This study demonstrates that both surface orientations together with the surface terminations of binary compounds can largely affect the atomistic structures of interfaces (see Sec. 3), which in turn determine the interfacial lattice coherence, the thermodynamic stability of interfaces and the mechanical stability of such interfaces in LMBs and solid-state batteries. Several studies have revealed the crucial role played by surface terminations of SEs in determining the interfacial stability.[11,53,54] For example, using first-principles calculations, Tateyama et al.[53] reported that the low-energy $Li_7La_3Zr_2O_{12}$ (LLZO) surfaces lead to the chemical instability of the LLZO‖Li-metal interface.

Our analysis also suggests that $W_{adhesion}$ (of eqn (4))—measuring the energy cost to separate two materials of a heterogeneous interface—is an important descriptor to evaluate the mechanical stability of interfaces.

In particular, $W_{adhesion}$ should be large enough to avoid interface delamination.[55] Yang et al. demonstrated that for common Li-metal‖SE interfaces, a $W_{adhesion} > 0.7$ J m^{-2} was required to prevent the formation of interfacial voids with the application of an external pressure of 20–30 MPa.[29] Recently, Seymour and Aguadero[28] have developed a "bond breaking" approach and derived that if $W_{adhesion} > 2\gamma$ (where γ is the surface energy of Li or Na metal), the formation of interfacial voids with potential loss of contact during Li (or Na) stripping could be avoided. Our data suggest that among the Li-based interfaces (Table S4†), only the $Li(100)\|Li_2O(110)$, $Li(100)\|Li_3N(110)$ and $Li(110)\|Li_3N(110)$ interfaces satisfy this criterion. For interfaces with Na metal, only the two $Na\|Na_2O$ interfaces have a $W_{adhesion}$ larger than twice the surface energy of Na(110) (or Na(100)).

The mechanisms of LiPON passivation of Li metal has been a matter of debate.[23,24,32] Recent studies by Hood et al.[23] have indicated that Li_3N and Li_2O are distributed uniformly on the surface of Li metal, while Li_3P was not in direct contact with Li metal. In contrast, the study led by the Meng research group had suggested that only Li_3N, Li_2O and Li_3PO_4 could be present in the interfacial region formed between Li-metal and LiPON.[24] Our results show that $Li\|Li_2O$ and $Li\|Li_3N$ interfaces have better interfacial stabilities than $Li\|Li_3P$, which agree well with the experimental scenario that both Li_2O and Li_3N can be in direct contact with Li metal, while Li_3P can only exist in the sub-interfacial layer.[23]

It has been established that argyrodite SEs are prone to decomposition against Li metal,[14,52] with evidence of formation of Li_2S, Li_3P and LiX (with X = Cl, Br or I) at the potential of Li metal (i.e., 0 volts vs. Li/Li^+). Among the interfaces formed between Li metal and the decomposition products of argyrodite

Li_6PS_5Cl as SE, i.e. $Li\|Li_2S$, $Li\|Li_3P$ and $Li\|LiCl$, $Li\|Li_3P$ has the largest value of $W_{adhesion}$ (Fig. 2), suggesting that Li_3P is more likely to form a stable interface with Li metal as compared to the other binary compounds. On one hand, the appreciable electronic conductivity of Li_3P could lead to continuous reactions with Li metal and growth of the decomposing interphases.[56] On the other hand, we have not considered the interfacial stability between binary compounds and Li_6PS_5Cl. Because these interfaces may not be mechanically stable, loss of contact between the SE and its decomposition products may also contribute to increased impedance.[14,22] Indeed, it has been shown that the change in particle size of Li_2S upon lithiation leads to loss of contact of the $Li_6PS_5Cl\|Li_2S$ interface and increases resistance.[25]
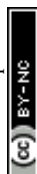
The Li^+ conductivity (or diffusivity) determined in experiments largely depends on the sample quality, its crystallinity and experimental conditions. In particular, the presence of defects, grain boundaries, and lattice disorder all affect Li^+ transport significantly.[57,58] Therefore, here we have restricted our study to the crystalline structures (both decomposing products and interfaces), a situation where the MTP approach has been proven to be adequate to predict ionic transport properties.[52,59,60] However, one major limitation of the current implementation of MTP is its lack of transferability from training within the binary bulk systems to being directly used in heterogeneous interfaces, requiring significant retraining of MTP with new training sets for each distinct interface. Therefore, a complete retraining of the MTP for each interface combination considered in this work is highly resource intensive, which pushes a comprehensive examination of Li (and Na) transport across all interfaces out of the scope of our work.

Assume that Li_6PS_5Cl reacts entirely with Li metal (at 0 volts vs. Li/Li^+) according to eqn (8):[14,15,52]

$$Li_6PS_5Cl + 8Li \rightarrow 5Li_2S + Li_3P + LiCl \quad (8)$$
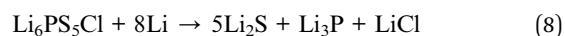
where Li_2S is produced $5\times$ in excess over the other binaries, in agreement with experimental evidence.[14,22] For example, from X-ray photoemission spectroscopy (XPS) experiments, Wenzel et al.[14] and Schwietert et al.[22] have observed the presence of Li_2S, LiCl, and Li_3P at the argyrodite‖Li-metal interface. On the basis of our interfacial energetics, Li^+ transport calculations and eqn (8), we propose a macroscopic picture of the interface of decomposing argyrodite-Li_6PS_5Cl against Li metal, as shown in Fig. 5.

Our data suggest a lower stability of the LiCl‖Li-metal interface as compared to Li_3P and Li_2S, which indicates that LiCl may be in direct contact with Li metal over a negligible interfacial area. It appears that LiCl may not be directly involved in interfacial Li-transport. At voltages larger than 0.0 volts vs. Li/Li^+ other decomposition products have been reported and observed, with the most prominent being Li_3PS_4,[15,20,22] which may form in the sub-interfacial layers of the SE. Since Li_2S is in molar excess over Li_3P and LiCl, the Li-ion percolation in the proximity of the metal electrode‖SE interfaces will be largely limited by the lower ionic conductivity of Li_2S.[14] Furthermore, our explicit study on interfaces confirmed that only Li metal‖Li_3P displays facile Li-ion
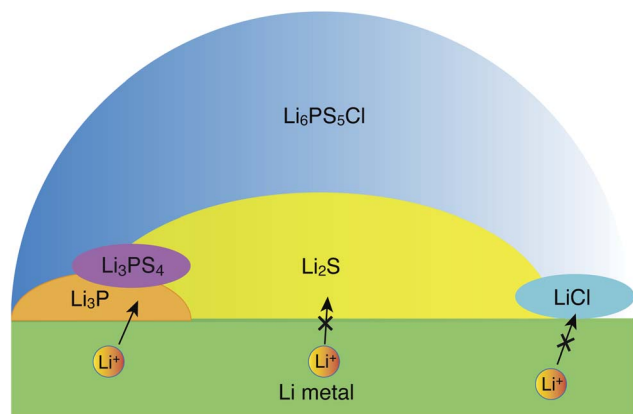
19738 | J. Mater. Chem. A, 2022, **10**, 19732–19742

This journal is © The Royal Society of Chemistry 2022

Fig. 5 Schematic illustration of a possible structure of the interface between Li metal and argyrodite-Li_6PS_5Cl, as inferred from the interfacial energetics and Li-ion transport simulations.

transport (Fig. 4c) as signified by the black arrows in Fig. 5, while the interfaces of Li metal with Li_2S and LiCl are resistive to Li-ion transport (Fig. 4 and S9†). Therefore, our qualitative results suggest that the decomposing interfaces are resistive to Li-ion transport as compared to the unreacted argyrodite SE.[14] Note that the interfaces formed among different decomposition products (e.g., $Li_3P \| Li_2S$) or the decomposition products with a solid electrolyte (e.g., Li_6PS_5Cl) are also of crucial importance to Li-ion transport. Therefore, explicit studies of these interfaces using high-fidelity machine learned potentials are certainly needed.

6 Conclusion

Chalcogen-containing SEs show among the highest room temperature ionic conductivities ($\sim 10^{-2}$ S cm^{-1}), but their practical applications in LMBs are limited by the decomposing interfaces when in contact with Li metal. Similar constraints bottleneck the implementation of SEs in NIBs as well. Therefore, it is vital to understand the interfacial properties of these decomposing interfaces, either experimentally or theoretically. In this work, we have systematically evaluated the thermodynamic stability (of Li- and Na-systems) and Li-ion transport properties of multiple decomposing interfaces, by employing first-principles calculations and large-scale MD simulations based on MLPs. Our results reveal that the interfacial stability of decomposition products with alkali-metals is largely affected by the surface properties of the decomposition products. In general, we have observed that the interfaces formed between alkali-metal with argyrodite-Li_6PS_5Cl are resistive to Li-ion transport. Finally, our high-fidelity MLPs, trained explicitly for interfaces, shed light on the complicated interfacial transport properties, which will aid in the study and optimization of SEs in the future.

7 Methods

7.1 First-principles calculations

DFT was used to approximate the energy contributions introduced in Sec. 2. The wavefunctions were described using plane-

waves for the valence electrons together with projected augmented wave potentials for the core electrons as implemented in the Vienna *Ab initio* Simulation Package (VASP).[61–63] The exchange–correlation contributions were treated within the generalized gradient approximation (GGA) as parameterized by Perdew, Burke, and Ernzerhof (PBE).[64] The valence electron configurations for each element were as follows: Li: $s^1 p^0$, N: $s^2 p^3$, O: $s^2 p^4$, Na: $s^1 p^0$, P: $s^2 p^3$, S: $s^2 p^4$ and Cl: $s^2 p^5$. The parameters we used for geometry optimization, surface energy and interfacial energetics calculations of the binary compounds and the constructed interfaces follow the MITRelaxSet, as in pymatgen.[65] We used a plane wave energy cutoff of 520 eV and a k-point mesh generated using a k-point density of 25 Å^{-1}. The total energy of each structure was converged to 10^{-5} eV per cell, and the geometry optimizations were stopped when the change in the total energy between two subsequent ionic steps was smaller than 10^{-4} eV.

AIMD simulations were performed with the VASP to generate the initial training sets for the MTP-MD (see Sec. 7.2). A plane-wave energy cutoff of 400 eV and a Γ-only k-mesh were used. The canonical ensemble (*NVT*) was achieved using a Nosé–Hoover thermostat and a time step of 2 fs.[66,67] Since previous studies have reported[59,68] that the training set for MTP-MD should cover the whole configurational space and contain sufficient data so as to rarely invoke DFT calculations, we performed AIMD calculations at 1000 K for 14–20 ps (preceded by a temperature ramping of 2 ps), which resulted in training sets containing 7000–10 000 configurations. The supercell sizes used for binary compound pristine structures were $4 \times 4 \times 4$ for Li metal (128 atoms), $2 \times 2 \times 2$ for Li_2S (96 atoms), $3 \times 3 \times 3$ for Li_3P (216 atoms) and $3 \times 3 \times 3$ for LiCl (216 atoms). We also studied vacancy-mediated diffusion by creating Li^+ vacancies inside the Li metal and binary compounds.

Li^+ vacancies were introduced by removing Li atoms and compensating for them with a uniform (jellium) charge background. Also, we created specific supercells that enabled a Li^+ vacancy concentration of $\sim 0.8\%$ for all compounds, which can arise at a synthesis temperature of 1200 K with a defect formation energy of 0.5 eV. Specifically, we used supercells of $4 \times 4 \times 4$ with one Li^+ vacancy for Li metal (127 atoms), $2 \times 2 \times 4$ with one Li^+ vacancy for Li_2S (191 atoms), $3 \times 3 \times 3$ with one Li^+ vacancy for Li_3P (215 atoms) and $3 \times 3 \times 3$ with one Li^+ vacancy for LiCl (215 atoms). To study Li^+ transport across Li-metal-∥decomposition product interfaces, we have created Li^+ vacancies randomly in the interface region (shaded regions in Fig. 2 and 4), with a vacancy concentration of $\sim 1.1\%$. The interfaces that we chose were $Li(110) \| Li_2S(110)$ (520 atoms), $Li(100) \| Li_3P(001)$ (406 atoms) and $Li(110) \| LiCl(100)$ (439 atoms).

7.2 Moment-tensor potential molecular dynamics

MTPs for the bulk and interfaces investigated in this study were trained using the machine learning of interatomic potentials (MLIP) package.[69] In the training of the MTP potentials, several parameters need to be carefully selected to balance computational cost *vs.* accuracy of the trained potentials. During training, we have extensively tested the effects of weights on

This journal is © The Royal Society of Chemistry 2022

J. Mater. Chem. A, 2022, **10**, 19732–19742 | **19739**

reproducing the *ab initio* total energies, forces and stresses, as well as the cutoff radius (R_{cut}) and the maximum level of basis functions (lev_{max}) on the accuracy of energy and forces of trained MTP potentials. We concluded that a ratio of weights of 100 : 10 : 1 for energies, forces, and stresses, respectively, was appropriate to achieve good accuracy. Also, we found that a lev_{max} of 10 and a R_{cut} of 5 Å, provided a tolerable level of fitting and validation errors in energies (<10 meV per atom) and forces (<30 meV Å^{-1}), as documented in Table S6.†

Since our MTPs were trained at high temperatures (~1000 K), we further validated the transferability of the potentials to lower temperatures (*i.e.*, 300–500 K). Specifically, we constructed validation sets by performing AIMD at 300 K/500 K for 4 ps (~2000 snapshots for each temperature). The fitting and validation errors on the total energies in both binary compounds and interface models were always <10 meV, while the errors on forces were within ~30 meV Å^{-1}.

Upon training, MTP-MD simulations were performed using LAMMPS,[70] where the MD simulations were performed in the temperature range of 300–1000 K at intervals of 100 K. A Nosé–Hoover thermostat was used to simulate the canonical ensemble (*NVT*).[66,67] Long MD simulations were carried out for at least 10 ns with a short time step of 1 fs, preceded by a temperature ramping for 100 ps and an equilibration period of 1 ns to reach each target temperature. We also benchmarked our MTP D^* data with AIMD results (see Table S9†). Specifically, we find that our MTP-MD calculated D^* at 900 K and 800 K are in reasonable agreement with AIMD calculations at the same temperatures, signifying the high fidelity of our MTP-MD simulations. The trained moment tensor potentials for both binary compounds and interface models are publicly available in the repository https://github.com/caneparesearch/MTP-Li_interface_binaries.git.

7.3 Error analysis of lithium ion diffusivity

To attain a better estimate of the computed Li-ion diffusivity and activation energy, we have considered the statistical variance of tracer diffusivity, $D^*(T)$ and performed a weighted linear least squares regression, following He *et al.* methodology.[71] In our Arrhenius plot, the weight of each point is determined by using the reciprocal of the variance of log $D^*(T)$. The variance of log $D^*(T)$ is calculated based on the propagation of uncertainty using eqn (9):

$$\sigma(\log D^*(T))^2 = \frac{\sigma\left(D^*(T)^2\right)}{D^*(T)^2} \tag{9}$$

where σ is the standard deviation of $D^*(T)$. We have divided the entire MD simulation into multiple non-overlapping MD sections, from which σ is determined. To minimize σ, we have tried dividing the MD simulations into different numbers of sections. For example, in LiCl we have computed σ for different numbers of sections, such as 10 ($\sigma = 1.48 \times 10^{-8}$ cm^2 s^{-1}), 100 (2.13×10^{-8}) and 1000 (6.73×10^{-8}). Clearly, larger numbers of sections increase σ; in this study, we have chosen 10 sections.

7.4 Validation of interfacial models

To verify the accuracy of our methodology in predicting interfacial properties, we have calculated interfacial energetics using two additional "constrained" optimization methods, namely, (i) "Fix-binary": the middle layers of the decomposition product was fixed to mimic the bulk in-plane lattice constants of the binary compound, and, (ii) "Fix-metal": middle layers of Li(Na) metal are fixed. The default method used throughout the work is when we do not constrain the middle layers of either binary compounds or the metal, referred to as "Fully-relaxed". To test these scenarios, we chose Na(110)‖Na$_2$O(110) for Na-based and Li(100)‖Li$_3$P(001) for Li-based interfaces, respectively. The calculated E_f, with and without constrained optimization, are shown in Fig. S6.† Notably, E_f calculated using constrained optimization is ~0.02 J m^{-2} and ~0.1 J m^{-2} higher than that of Fully-relaxed for Li(100)‖Li$_3$P(001), and Na(110)‖Na$_2$O(110), respectively.

Another typically used approach for calculating interfacial energy σ excluding the strain effect is to compute interface formation energy at varied slab thicknesses of Li (or Na) metal, and σ is obtained by taking the y-intercept of the extrapolated value of E_f.[26] To test this approach, we have taken Li(100)‖Li$_3$P(001) and Li(110)‖Li$_2$S interfaces which are used later to investigate Li-ion transport. We fixed the in-plane lattice constants of the interfaces to that of the binary compounds, while varying the number of Li-metal slabs. We find that in both cases, the variations of E_f with different formula units of Li-metal slab (denoted as n_{Li}) are not significant (see Fig. S10†). This indicates that the strain energy is not very sensitive to the system size. Using both approaches, the Li(100)‖Li$_3$P(001) interface appears consistently more stable than the Li(110)‖Li$_2$S interface.

Conflicts of interest

There are no conflicts to declare.

Acknowledgements

Notes and references

1 J. B. Goodenough and Y. Kim, *Chem. Mater.*, 2010, **22**, 587–603.
2 W. Xu, J. Wang, F. Ding, X. Chen, E. Nasybulin, Y. Zhang and J.-G. Zhang, *Energy Environ. Sci.*, 2014, **7**, 513–537.
3 D. Lin, Y. Liu and Y. Cui, *Nat. Nanotechnol.*, 2017, **12**, 194–206.
4 T. Krauskopf, F. H. Richter, W. G. Zeier and J. Janek, *Chem. Rev.*, 2020, **120**, 7745–7794.

19740 | *J. Mater. Chem. A*, 2022, **10**, 19732–19742

This journal is © The Royal Society of Chemistry 2022

5 X.-B. Cheng, R. Zhang, C.-Z. Zhao and Q. Zhang, *Chem. Rev.*, 2017, **117**, 10403–10473.

6 C. Fang, B. Lu, G. Pawar, M. Zhang, D. Cheng, S. Chen, M. Ceja, J.-M. Doux, H. Musrock, M. Cai, B. Liaw and Y. S. Meng, *Nat. Energy*, 2021, **6**, 987–994.

7 K. Xu, *Chem. Rev.*, 2004, **104**, 4303–4418.

8 N. Yabuuchi, K. Kubota, M. Dahbi and S. Komaba, *Chem. Rev.*, 2014, **114**, 11636–11682.

9 P. K. Nayak, L. Yang, W. Brehm and P. Adelhelm, *Angew. Chem., Int. Ed.*, 2018, **57**, 102–120.

10 C. Delmas, *Adv. Energy Mater.*, 2018, **8**, 1703137.

11 J. Haruyama, K. Sodeyama, L. Han, K. Takada and Y. Tateyama, *Chem. Mater.*, 2014, **26**, 4248–4255.

12 H. Tang, Z. Deng, Z. Lin, Z. Wang, I.-H. Chu, C. Chen, Z. Zhu, C. Zheng and S. P. Ong, *Chem. Mater.*, 2018, **30**, 163–173.

13 E. A. Wu, C. S. Kompella, Z. Zhu, J. Z. Lee, S. C. Lee, I.-H. Chu, H. Nguyen, S. P. Ong, A. Banerjee and Y. S. Meng, *ACS Appl. Mater. Interfaces*, 2018, **10**, 10076–10086.

14 S. Wenzel, S. J. Sedlmaier, C. Dietrich, W. G. Zeier and J. Janek, *Solid State Ionics*, 2018, **318**, 102–112.

15 W. D. Richards, L. J. Miara, Y. Wang, J. C. Kim and G. Ceder, *Chem. Mater.*, 2016, **28**, 266–273.

16 B. Gao, R. Jalem and Y. Tateyama, *ACS Appl. Mater. Interfaces*, 2021, **13**, 11765–11773.

17 T. Famprikis, P. Canepa, J. A. Dawson, M. S. Islam and C. Masquelier, *Nat. Mater.*, 2019, **18**, 1278–1291.

18 T. Famprikis, Ö. U. Kudu, J. A. Dawson, P. Canepa, F. Fauth, E. Suard, M. Zbiri, D. Dambournet, O. J. Borkiewicz, H. Bouyanfif, S. P. Emge, S. Cretu, J.-N. Chotard, C. P. Grey, W. G. Zeier, M. S. Islam and C. Masquelier, *J. Am. Chem. Soc.*, 2020, **142**, 18422–18436.

19 L. Baggetto, R. A. H. Niessen, F. Roozeboom and P. H. L. Notten, *Adv. Funct. Mater.*, 2008, **18**, 1057–1066.

20 Y. Zhu, X. He and Y. Mo, *J. Mater. Chem. A*, 2016, **4**, 3253–3266.

21 V. Lacivita, Y. Wang, S.-H. Bo and G. Ceder, *J. Mater. Chem. A*, 2019, **7**, 8144–8155.

22 T. K. Schwietert, V. A. Arszelewska, C. Wang, C. Yu, A. Vasileiadis, N. J. J. de Klerk, J. Hageman, T. Hupfer, I. Kerkamm, Y. Xu, E. van der Maas, E. M. Kelder, S. Ganapathy and M. Wagemaker, *Nat. Mater.*, 2020, **19**, 428–435.

23 Z. D. Hood, X. Chen, R. L. Sacci, X. Liu, G. M. Veith, Y. Mo, J. Niu, N. J. Dudney and M. Chi, *Nano Lett.*, 2021, **21**, 151–157.

24 D. Cheng, T. A. Wynn, X. Wang, S. Wang, M. Zhang, R. Shimizu, S. Bai, H. Nguyen, C. Fang, M.-c. Kim, W. Li, B. Lu, S. J. Kim and Y. S. Meng, *Joule*, 2020, **4**, 2484–2500.

25 C. Yu, S. Ganapathy, N. J. J. de Klerk, I. Roslon, E. R. H. van Eck, A. P. M. Kentgens and M. Wagemaker, *J. Am. Chem. Soc.*, 2016, **138**, 11192–11201.

26 N. D. Lepley and N. A. W. Holzwarth, *Phys. Rev. B: Condens. Matter Mater. Phys.*, 2015, **92**, 214201.

27 C.-T. Yang and Y. Qi, *Chem. Mater.*, 2021, **33**, 2814–2823.

28 I. D. Seymour and A. Aguadero, *J. Mater. Chem. A*, 2021, **9**, 19901–19913.

29 M. Yang, Y. Liu, A. M. Nolan and Y. Mo, *Adv. Mater.*, 2021, **33**, 2008081.

30 F. Mizuno, A. Hayashi, K. Tadanaga and M. Tatsumisago, *Adv. Mater.*, 2005, **17**, 918–921.

31 T. Hakari, M. Nagao, A. Hayashi and M. Tatsumisago, *J. Power Sources*, 2015, **293**, 721–725.

32 A. Schwöbel, R. Hausbrand and W. Jaegermann, *Solid State Ionics*, 2015, **273**, 51–54.

33 P. W. Tasker, *J. Phys. C: Solid State Phys.*, 1979, **12**, 4977–4984.

34 K. T. Butler, G. Sai Gautam and P. Canepa, *npj Comput. Mater.*, 2019, **5**, 19.

35 T. Einstein, *Handbook of Crystal Growth*, Elsevier, 2015, pp. 215–264.

36 R. Tran, Z. Xu, B. Radhakrishnan, D. Winston, W. Sun, K. A. Persson and S. P. Ong, *Sci. Data*, 2016, **3**, 160080.

37 Y.-X. Chen and P. Kaghazchi, *Nanoscale*, 2014, **6**, 13391–13395.

38 W. C. Mackrodt, *J. Chem. Soc., Faraday Trans. 2*, 1989, **85**, 541.

39 Z. Liu, Y. Qi, Y. X. Lin, L. Chen, P. Lu and L. Q. Chen, *J. Electrochem. Soc.*, 2016, **163**, A592–A598.

40 A. Hashibon, C. Elsasser and M. Ruhle, *Acta Mater.*, 2005, **53**, 5323–5332.

41 R. Benedek, D. N. Seidman and C. Woodward, *J. Phys.: Condens. Matter*, 2002, **14**, 2877–2900.

42 A.-L. Dalverny, J.-S. Filhol and M.-L. Doublet, *J. Mater. Chem.*, 2011, **21**, 10134.

43 N. T. Taylor, F. H. Davies, I. E. M. Rudkin, C. J. Price, T. H. Chan and S. P. Hepplestone, *Comput. Phys. Commun.*, 2020, **257**, 107515.

44 Z. Deng, Z. Wang, I.-H. Chu, J. Luo and S. P. Ong, *J. Electrochem. Soc.*, 2016, **163**, A67–A74.

45 A. Kato, H. Kowada, M. Deguchi, C. Hotehama, A. Hayashi and M. Tatsumisago, *Solid State Ionics*, 2018, **322**, 1–4.

46 Y. Xiao, Y. Wang, S.-H. Bo, J. C. Kim, L. J. Miara and G. Ceder, *Nat. Rev. Mater.*, 2020, **5**, 105–126.

47 J. Bates, *Solid State Ionics*, 1992, **53–56**, 647–654.

48 A. V. Shapeev, *Multiscale Model. Simul.*, 2016, **14**, 1153–1173.

49 R. Court-Castagnet, *Solid State Ionics*, 1993, **61**, 327–334.

50 G. Nazri, *Solid State Ionics*, 1989, **34**, 97–102.

51 F. Altorfer, W. Bührer, I. Anderson, O. Schärpf, H. Bill, P. Carron and H. Smith, *Phys. B*, 1992, **180–181**, 795–797.

52 C. Wang, K. Aoyagi, M. Aykol and T. Mueller, *ACS Appl. Mater. Interfaces*, 2020, **12**, 55510–55519.

53 B. Gao, R. Jalem and Y. Tateyama, *ACS Appl. Mater. Interfaces*, 2020, **12**, 16350–16358.

54 H.-K. Tian, R. Jalem, B. Gao, Y. Yamamoto, S. Muto, M. Sakakura, Y. Iriyama and Y. Tateyama, *ACS Appl. Mater. Interfaces*, 2020, **12**, 54752–54762.

55 A. Wang, S. Kadam, H. Li, S. Shi and Y. Qi, *npj Comput. Mater.*, 2018, **4**, 15.

56 P. Gorai, T. Famprikis, B. Singh, V. Stevanović and P. Canepa, *Chem. Mater.*, 2021, **33**, 7484–7498.

57 V. Lacivita, N. Artrith and G. Ceder, *Chem. Mater.*, 2018, **30**, 7077–7090.

This journal is © The Royal Society of Chemistry 2022

J. Mater. Chem. A, 2022, **10**, 19732–19742 | **19741**

58 E. Sebti, H. A. Evans, H. Chen, P. M. Richardson, K. M. White, R. Giovine, K. P. Koirala, Y. Xu, E. Gonzalez-Correa, C. Wang, C. M. Brown, A. K. Cheetham, P. Canepa and R. J. Clément, *J. Am. Chem. Soc.*, 2022, **144**, 5795–5811.

59 C. Wang, K. Aoyagi, P. Wisesa and T. Mueller, *Chem. Mater.*, 2020, **32**, 3741–3752.

60 J. Qi, S. Banerjee, Y. Zuo, C. Chen, Z. Zhu, M. Holekevi Chandrappa, X. Li and S. Ong, *Mater. Today Phys.*, 2021, **21**, 100463.

61 P. E. Blöchl, *Phys. Rev. B: Condens. Matter Mater. Phys.*, 1994, **50**, 17953–17979.

62 G. Kresse and D. Joubert, *Phys. Rev. B: Condens. Matter Mater. Phys.*, 1999, **59**, 1758–1775.

63 G. Kresse and J. Furthmüller, *Phys. Rev. B: Condens. Matter Mater. Phys.*, 1996, **54**, 11169–11186.

64 J. P. Perdew, K. Burke and M. Ernzerhof, *Phys. Rev. Lett.*, 1996, **77**, 3865–3868.

65 S. P. Ong, W. D. Richards, A. Jain, G. Hautier, M. Kocher, S. Cholia, D. Gunter, V. L. Chevrier, K. A. Persson and G. Ceder, *Comput. Mater. Sci.*, 2013, **68**, 314–319.

66 S. Nosé, *J. Chem. Phys.*, 1984, **81**, 511–519.

67 W. G. Hoover, *Phys. Rev. A: At., Mol., Opt. Phys.*, 1985, **31**, 1695–1697.

68 I. Novoselov, A. Yanilkin, A. Shapeev and E. Podryabinkin, *Comput. Mater. Sci.*, 2019, **164**, 46–56.

69 E. V. Podryabinkin and A. V. Shapeev, *Comput. Mater. Sci.*, 2017, **140**, 171–180.

70 S. Plimpton, *J. Comput. Phys.*, 1995, **117**, 1–19.

71 X. He, Y. Zhu, A. Epstein and Y. Mo, *npj Comput. Mater.*, 2018, **4**, 18.